Monthly Notices
of the
ROYAL ASTRONOMICAL SOCIETY

MNRAS **527,** 2094–2109 (2024)
Advance Access publication 2023 October 6

https://doi.org/10.1093/mnras/stad3057

Formation of misaligned second-generation discs through fly-by encounters

Jeremy L. Smallwood ,[1]★ Rebecca Nealon ,[2,3] Nicolás Cuello,[4] Ruobing Dong (董若冰)[1,5] and Richard A. Booth [6]

[1] *Institute of Astronomy and Astrophysics, Academia Sinica, Taipei 10617, Republic of China*
[2] *Centre for Exoplanets and Habitability, University of Warwick, Coventry CV4 7AL, UK*
[3] *Department of Physics, University of Warwick, Coventry CV4 7AL, UK*
[4] *IPAG, CNRS, Université Grenoble Alpes, F-38000 Grenoble, France*
[5] *Department of Physics and Astronomy, University of Victoria, Victoria, BC V8P 5C2, Canada*
[6] *School of Physics and Astronomy, University of Leeds, Leeds LS2 9JT, UK*

Accepted 2023 October 3. Received 2023 September 4; in original form 2023 July 12

ABSTRACT

Observations reveal protoplanetary discs being perturbed by fly-by candidates. We simulate a scenario where an unbound perturber, i.e. a fly-by, undergoes an inclined grazing encounter, capturing material and forming a second-generation protoplanetary disc. We run *N*-body and three-dimensional hydrodynamical simulations of a parabolic fly-by grazing a particle disc and a gas-rich protoplanetary disc, respectively. In both our *N*-body and hydrodynamic simulations, we find that the captured, second-generation disc forms at a tilt twice the initial fly-by tilt. This relationship is robust to variations in the fly-by's tilt, position angle, periastron, and mass. We extend this concept by also simulating the case where the fly-by has a disc of material prior to the encounter but we do not find the same trend. An inclined disc with respect to the primary disc around a misaligned fly-by is tilted by a few degrees, remaining close to its initial disc tilt. Therefore, if a disc is present around the fly-by before the encounter, the disc may not tilt up to twice the perturber tilt depending on the balance between the angular momentum of the circumsecondary disc and captured particles. In the case where the perturber has no initial disc, analysing the orientation of these second-generation discs can give information about the orbital properties of the fly-by encounter.

Key words: hydrodynamics – methods: numerical – planets and satellites: formation – protoplanetary discs.

1 INTRODUCTION

Recent observations of protoplanetary discs reveal disc substructures, such as rings, gaps, and spirals (Andrews 2020; van der Marel et al. 2021). Disc substructures can be excited from either bound or unbound companions, suggesting that these substructures can be used as a signpost for planet formation (Grady et al. 1999, 2013; Muto et al. 2012; Wagner et al. 2015; Monnier et al. 2019; Garufi et al. 2020; Muro-Arena et al. 2020). Stars born in dense stellar clusters are subject to stellar fly-by events (Pfalzner 2013), where a companion on an unbound orbit can perturb protoplanetary discs (Clarke & Pringle 1993; Cuello, Ménard & Price 2023). Studying the long-term effects of a fly-by encounter on the protoplanetary disc structure can shed light on understanding observations.

A perturber on a fly-by or unbound orbit is defined as having a single periastron passage within 1000 au. The probability of stellar fly-by events is enhanced in dense stellar clusters, where the chance of stellar encounters is high (Hillenbrand 1997; Carpenter 2000; Lada & Lada 2003; Porras et al. 2003). From the works of Pfalzner (2013), and Winter et al. (2018a), stellar fly-bys encounter a solar-type star within the first million years of stellar evolution at a probability of 30 per cent for a background stellar density that is larger than in Taurus. Recently, Pfalzner & Govind (2021) found that the frequency of close fly-bys in low-mass clusters is underestimated and that low-mass clusters should contain 10 per cent – 15 per cent of discs smaller than 30 au truncated by fly-bys. The hydrodynamical studies of star formation from dense stellar clusters by Bate (2018) reported that most stellar encounters occur with the first Myr of stellar evolution, consistent with previous works. Parabolic orbit encounters are found to be more probable than hyperbolic orbits (see fig. 7 in Pfalzner 2013). The lifetime of gaseous protoplanetary discs is estimated to be 1 – 10 Myr (Haisch, Lada & Lada 2001; Hernández et al. 2007, 2008; Mamajek 2009; Ribas, Bouy & Merín 2015). Therefore, fly-by events have the potential to perturb and shape protoplanetary discs (Cuello et al. 2019, 2020; Jiménez-Torres 2020; Ménard et al. 2020). For example, unbound encounters can truncate protoplanetary discs, which can influence the total size and occurrence rate of planetary systems (e.g. Scally & Clarke 2001; Adams et al. 2006; Olczak, Pfalzner & Spurzem 2006; Rosotti et al. 2014; Steinhausen & Pfalzner 2014; Portegies Zwart 2016; Vincke & Pfalzner 2016; Concha-Ramírez et al. 2019, 2021; Jiménez-Torres 2020). Stellar fly-bys can enhance photoevaporation of protoplanetary discs, which can ultimately decrease the gaseous disc lifetime (Dai et al. 2018; Winter et al. 2018a).

★ E-mail: jlsmallwood@asiaa.sinica.edu.tw

There are several observed fly-by candidates that are undergoing interactions with protoplanetary discs, such as RW Aur (Cabrit et al. 2006; Dai et al. 2015; Rodriguez et al. 2018), AS 205 (Kurtovic et al. 2018), HV Tau and Do Tau (Winter, Booth & Clarke 2018b), FU Ori (Beck & Aspin 2012; Takami et al. 2018; Pérez et al. 2020; Borchert et al. 2022a, b), Z CMa (Takami et al. 2018; Dong et al. 2022), UX Tau (Ménard et al. 2020), and Sgr C (Lu et al. 2022). The systems V2775 Ori (Zurlo et al. 2017) and V1647 Ori (Principe et al. 2018) are highly speculative to be fly-by encounters. For a recent review on fly-by's shaping protoplanetary discs, see Cuello et al. (2023).

When the perturber approaches periastron passage, tidal effects by the perturber excites the formation of spirals and potentially disc fragmentation (Ostriker 1994; Pfalzner 2003; Shen et al. 2010; Thies et al. 2010; Smallwood et al. 2023). External unbound companions will excite spiral density waves at Lindblad, and corotation resonances (e.g. Lin & Papaloizou 1993). If the unbound companion is an external star, it exerts a strong tidal force where its Roche lobe can reach beyond the location of most of these resonances. Furthermore, fly-by events can warp the primary disc for a range of perturber inclinations and periastron distances (Clarke & Pringle 1993; Ostriker 1994; Terquem & Bertout 1996; Bhandare, Breslau & Pfalzner 2016; Xiang-Gruess 2016). Aside from spiral formation, long bridges of material are linked from the primary disc to the intruding fly-by (Cuello et al. 2019, 2020). Warps and misalignments are typical in the primary disc and are observable in moment one maps (Cuello et al. 2020). Broken protoplanetary discs can have large mutual misalignments between the inner and outer gas rings generated by a fly-by scenario (Nealon, Cuello & Alexander 2020).

Clarke & Pringle (1993) demonstrated that a prograde, coplanar parabolic fly-by encounter stripped material off the protoplanetary disc, and the perturber captured a portion of the stripped material. Perturbers on hyperbolic trajectories ($e > 1$) have a higher angular velocity during periapsis, leaving a lesser mark on the primary disc structure (e.g. Winter et al. 2018b), and are less efficient in capturing material compared to parabolic encounters (e.g. Larwood & Papaloizou 1997; Pfalzner, Umbreit & Henning 2005b; Breslau, Vincke & Pfalzner 2017). Despite knowing that material can be captured during a fly-by encounter, the relationship between the inclination of the perturber and the captured material has not been investigated fully. Jílková et al. (2016) examined the distribution of captured material during a fly-by encounter through *N*-body simulations, however, they did not consider hydrodynamical discs. After the passage of the perturber has already occurred, we can still observe the second-generation disc. Therefore, if there is a relationship between the captured material and the fly-by, we can reconstruct the orbit of the fly-by and shed light on the many fly-by candidate observations. One observational example is UX Tau, where the disc around UX Tau C is thought to be captured during the encounter (Ménard et al. 2020).

In this work, we focus on the transfer of material from the primary protoplanetary disc to the unbound perturber, which forms a second-generation disc. We run three-dimensional *N*-body and hydrodynamical simulations of a parabolic fly-by interacting with a protoplanetary disc, tracking the formation and evolution of disc material around the fly-by. We find there is a strong relationship between the inclination of the captured material and the initial tilt of the perturber. By measuring the mutual inclination of the two discs and comparing them to observations, we can reconstruct the orbit of the observed fly-by candidate, deducing whether or not fly-by candidates are indeed on unbound orbits. The layout of the paper is as follows. Section 2 describes the numerical set-up routines for our *N*-body and hydrodynamical simulations to model a parabolic encounter interacting with a circumprimary disc. In Sections 3 and 4, we report the results of our *N*-body and hydrodynamical simulations, respectively. Section 5 shows hydrodynamical results of two interacting protoplanetary discs on parabolic orbits. Section 6 gives an analytical framework on how particles are captured during a fly-by encounter. In Section 7, we discuss how our results apply to observations of fly-by candidate systems. Finally, we give a conclusion in Section 8.

2 METHODS

We conduct two types of simulations. First, we consider a fly-by using an *N*-body code that does not take into account any pressure or viscous effects. Second, we confirm and expand on these results using hydrodynamic simulations. For the hydrodynamical simulations, we simulate a bound, parabolic, and hyperbolic encounter to test how the relative velocity between the perturber and disc affects the orientation of the captured disc around the perturber. For the *N*-body simulations, we only simulate a parabolic encounter. Here, we detail the important parameters for all of our simulations.

2.1 Parabolic orbit set-up

We describe the set-up of an unbound perturber that gravitationally influences the protoplanetary disc around the primary star. We simulate strictly parabolic encounters ($e \approx 1$), which induce the largest star-to-disc angular momentum transfer and produce the most prominent substructures in the disc (Vincke & Pfalzner 2016; Winter et al. 2018b; Cuello et al. 2019, 2020).

We use the same orbital set-up for our *N*-body and hydrodynamical simulations. In this work, we denote the host and fly-by with subscripts '1' and '2', respectively. A schematic of a perturber on a parabolic orbit encountering an accretion disc is given in Fig. 1. We model coplanar and inclined parabolic trajectories with the radial distance, r_2, described by

$$r_2 = \frac{2r_\mathrm{p}}{1+\sin\theta} \tag{1}$$

(Bate, Mueller & White 1971), where r_p is the periastron distance, and θ is the angle between periastron position vector and velocity vector. The periastron passage occurs at $\theta = +\pi/2$, where the velocity vector is perpendicular to the periastron position vector (see the right panel in Fig. 1). The angular speed as a function of r_2 is then

$$\omega(r_2) = \sqrt{\frac{2G(M_1+M_2)}{r_\mathrm{p}^3}}\left(\frac{r_\mathrm{p}}{r_2}\right)^2 \tag{2}$$

$$= \left(0.18\,^\circ\mathrm{yr}^{-1}\right)\left(\frac{M_1+M_2}{M_\odot}\right)^{1/2}\left(\frac{r_\mathrm{p}}{200\,\mathrm{au}}\right)^{-3/2}\left(\frac{r_\mathrm{p}}{r_2}\right)^2 \tag{3}$$

(Bate et al. 1971), where M_1 and M_2 are the masses of the primary and fly-by, respectively, and G is the gravitational constant. The relationship between the fly-by separation, r_2, and time t is given by

$$\left(\frac{r_2}{r_\mathrm{p}}+2\right)\sqrt{\frac{r_2}{r_\mathrm{p}}-1} = \frac{3|t-t_\mathrm{p}|}{2}\sqrt{\frac{2G(M_1+M_2)}{r_\mathrm{p}^3}}, \tag{4}$$

where $r_2 = r_\mathrm{p}$ when $t = t_\mathrm{p}$.

For a coplanar parabolic orbit, the perturber lies in the x–y plane, arrives initially from the negative y, positive x direction, and leaves towards the negative y, negative x direction. When we incline the orbit by an arbitrary amount, we rotate the orbit clockwise about the y-axis. Therefore, all coplanar and inclined models will have the

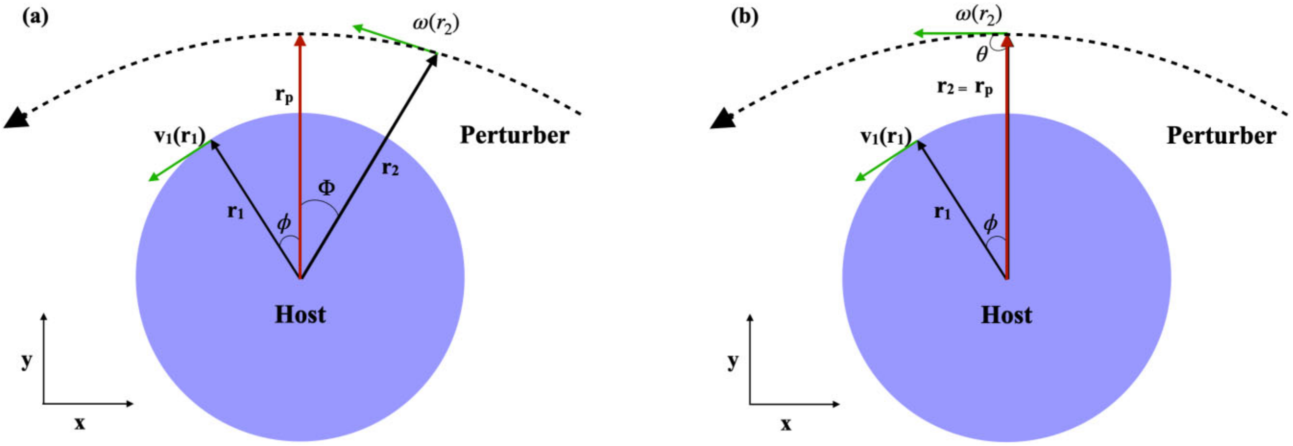

Figure 1. A schematic view of an accretion disc (the host) encountering a perturber on a parabolic orbit (dotted-black curve). The left panel shows before the closest approach and the right panel the instant of closest approach, used to define the terms in equation (1). The position vectors are given in black, with the exception of the periastron position vector which is given in red. The velocity vectors are given in green.

Table 1. A summary of the *N*-body simulations. The simulation ID is given in the first column. The tilt of the perturber is given in the second column, and the average tilt of the captured particles around the perturber with the standard error is given in the last column.

Simulation	i_2 (°)	$i_{\rm disc,\,2}$ (°)
N0	0	$\sim$0 ± 0.0
N15	15	$\sim$43 ± 0.521
N30	30	$\sim$63 ± 0.525
N45	45	$\sim$81 ± 0.667
N60	60	$\sim$113 ± 3.485

same perturber periastron (x, y, z) coordinate centred on the host star, unless the position angle of the orbit is non-zero.

2.2 *N*-body simulation set-up

We model a perturber on a parabolic orbit and a circumprimary disc of particles using the WHFAST integrator, which is a second-order symplectic Wisdom Holman integrator with 11th-order symplectic correctors in the *N*-body simulation package, REBOUND (Rein & Tamayo 2015). We construct a disc of 10 000 test particles around the primary star, with an inner disc radius $r_{\rm in} = 10$ au, and outer disc radius $r_{\rm out} = 100$ au. The test particles are initially on circular orbits and coplanar with respect to the x–y plane. The centre star has a mass $M_1 = 1\,{\rm M}_\odot$, and the perturber's mass is also set to $M_2 = 1\,{\rm M}_\odot$. The perturber's periastron distance is set to $r_{\rm p} = 200$ au, with an initial separation $r_0 = 500$ au. We model various simulations where parabolic orbit is tilted by $i_0 = 0^\circ, 15^\circ, 30^\circ, 45^\circ$, and 60°, see Table 1. For each particle in the simulation, we determine whether it is bound to the primary or secondary star by calculating the specific energies (kinetic plus potential). When the specific energies of the particles are negative, they are considered bound, and we then calculate the particle parameters (i.e. separation, eccentricity, and inclination) with respect to its bound companion. The inclination is measured by calculating the angle between the particle's angular momentum vector and the z-axis. Observationally, it is more useful to analyse the inclination from the z-axis as it indicates the angle by which the orbits have been inclined with respect to the initial state.

2.3 Hydrodynamical simulation set-up

We simulate a primary star surrounded by a gaseous protoplanetary disc and a parabolic fly-by encounter using the three-dimensional smoothed particle hydrodynamics (SPH) code PHANTOM (Price et al. 2018). PHANTOM has been extensively tested to simulate unbound encounters (Cuello et al. 2019, 2020; Ménard et al. 2020; Nealon et al. 2020; Borchert et al. 2022a, b; Smallwood et al. 2023). The code can model an assortment of parabolic orbit configurations such that the system's angular momentum is conserved with the same accuracy order as the time-stepping scheme. We only report encounters that result in a disc around the perturber.

2.3.1 *Primary star and protoplanetary disc set-up*

We set up a gas-only protoplanetary disc around a generic solar-type star that is initially coplanar to the spin-axis of the star, assumed to be the z-axis. We simulate the hydrodynamical disc in the bending wave regime, such that the disc aspect ratio H/r is larger than the Shakura & Sunyaev (1973) viscosity coefficient $\alpha_{\rm SS}$. The warp induced by the unbound perturber will propagate as a pressure wave with speed $\sim c_{\rm s}/2$ (Papaloizou & Pringle 1983; Papaloizou & Lin 1995), where $c_{\rm s}$ is the sound speed. The hydrodynamical disc is modelled as a flat disc with 500 000 Lagrangian particles with a total disc mass of $0.001\,{\rm M}_\odot$. We include one higher resolution simulation with 4×10^6 particles for a resolution study. During periastron passage of the fly-by, the low disc mass ensures that there is negligible gravitational effect imparted on to the fly-by from the disc and we can safely ignore the effect of disc self-gravity. The mass of the primary star is set to $M_1 = 1\,{\rm M}_\odot$. We set the inner disc radius to $r_{\rm in} = 10$ au and the outer radius is $r_{\rm out} = 100$ au. The primary star has an accretion radius of $r_{\rm acc,1} = 10$ au. We purposefully make the accretion radius equivalent to the initial inner edge of the disc to speed up computational time with not having to resolve close-in particle orbits. The accretion radius is a hard boundary such that any Lagrangian particles that penetrate the boundary are considered accreted, and the particle's mass, angular momentum, and linear momentum are deposited on to the sink.

The disc surface density profile is initially a power-law distribution given by

$$\Sigma(R) = \Sigma_0\left(\frac{r}{r_{\rm in}}\right)^{-p}, \tag{5}$$

where $\Sigma_0 = 7.00\,\mathrm{g\,cm^{-2}}$ is the density normalization, r is the radial distance in the disc, and p is the power-law index. We set $p = 1.5$, and the total disc mass defines the density normalization. Previous hydrodynamic simulations of fly-by–disc interactions used a radial surface density profile of $p = 1$ to match observed disc profiles (e.g. Cuello et al. 2019, 2020), which initially loads more material in the outer disc regions compared to $p = 1.5$. Since we select a low disc mass, the dynamical behaviour of the disc material during the encounter does not sensitively depend on the initial surface density profile. We use a locally isothermal equation of state with a disc thickness that is scaled with radius as

$$H = \frac{c_\mathrm{s}}{\Omega} \propto r^{3/2-q}, \tag{6}$$

where $\Omega = \sqrt{GM/r^3}$. The initial disc aspect ratio is $H/r = 0.05$ at r_in. The Shakura & Sunyaev (1973) viscosity prescription, denoted as α_SS, is given by

$$\nu = \alpha_\mathrm{SS} c_\mathrm{s} H, \tag{7}$$

where ν is the kinematic viscosity. To calculate α_SS, we follow the details given in Lodato & Price (2010), such that

$$\alpha_\mathrm{SS} \approx \frac{\alpha_\mathrm{AV}}{10} \frac{\langle h \rangle}{H}, \tag{8}$$

where $\langle h \rangle$ is the mean smoothing length of particles in a cylindrical ring at a given radius (Lodato & Price 2010). In this work, we set $\alpha_\mathrm{SS} = 0.005$, which translates to an artificial viscosity of $\alpha_\mathrm{AV} = 0.1260$ (0.2713 for the high-resolution simulation) (see Meru & Bate 2012, for details). We note that the α_AV is always higher than the suggested limit from Meru & Bate (2012). To prevent particle-particle penetration in the high Mach number regime, we include a term, β_AV (e.g. Monaghan 1989). Traditionally, $\beta_\mathrm{AV} = 2.0$ (Lodato & Pringle 2007; Price et al. 2018). The disc is resolved with a shell-averaged smoothing length per scale height of $\langle h \rangle/H \approx 0.5$ and $\langle h \rangle/H \approx 0.25$ for our high-resolution simulation.

To more accurately simulate the formation and development of discs around an unbound companion, we adopt the locally isothermal equation of state of Farris et al. (2014) and set the sound speed c_s to be

$$c_\mathrm{s} = c_\mathrm{s0} \left(\frac{r_2}{M_1 + M_2} \right)^q \left(\frac{M_1}{R_1} + \frac{M_2}{R_2} \right)^q, \tag{9}$$

where R_1 and R_2 are the radial distances from the primary and secondary stars, respectively, and c_s0 is a constant with dimensions of velocity and q is set to 3/4. This sound speed prescription guarantees that the primary and secondary stars set the temperature profiles in the circumprimary and circumsecondary discs, respectively. For R_1, $R_2 \gg r_2$, c_s is set by the distance from the centre of mass of the system.

2.3.2 *Perturber set-up*

We vary the mass, periastron distance, tilt, and position angle of the perturber. The standard perturber mass we select is $M_2 = 0.2\,\mathrm{M_\odot}$, however, we also use $M_2 = 1\,\mathrm{M_\odot}$. The total mass of the system is then $M_\mathrm{tot} = M_1 + M_2$. The standard periastron distance we select is $r_\mathrm{p} = 100$ au, in which case the fly-by is a grazing encounter. Simulations with the standard periastron distance will have the same periastron distance regardless of trajectory misalignment, which occurs at $x = 0$ and $y > 0$. We also consider periastron distances of $r_\mathrm{p} = 80,\ 120,$ au. The tilt of the fly-by orbit is measured with respect to the z-axis. The majority of the simulations model an inclined perturber trajectory being $i_2 = 45^\circ$, but we also consider fly-by orbits inclined by 0° (coplanar prograde), 15°, 30°, and 60°. A coplanar perturber initially lies in the x–y plane and arrives from the negative y direction, and leaves towards the negative y direction. The reference frame within our simulations is centred on the system's centre of mass. We also model a bound companion with eccentricities $e_2 = 0.3$ and $e_2 = 0.7$ with mass $M_2 = 0.2\,\mathrm{M_\odot}$. The bound companion initial begins at apastron. We simulate only a single orbital period that mimics a 'fly-by' encounter. The summary of the hydrodynamical simulations is given in Table 3.

2.3.3 *Perturber disc set-up*

In four simulations, PD0_0, PD45_0, PD45_0_light, and PD45_45, we include an initial circumsecondary disc around the perturber. These types of simulations aim to examine the transfer of material between two protoplanetary discs during a fly-by encounter. For these simulations, we set $r_\mathrm{p} = 100$ au and $M_2 = 0.2\,\mathrm{M_\odot}$. The circumsecondary disc mirrors the disc parameters of the primary disc (given in Section 2.3.1), however, the inner and outer disc radii are set to $r_\mathrm{in,2} = 3.3$ au and $r_\mathrm{out,2} = 33$ au, respectively. The inner radius is chosen to equal the accretion radius of the perturber. The outer radius is chosen based on the truncation radius of a binary system being about one-third of the separation (e.g. Artymowicz & Lubow 1994; Pichardo, Sparke & Aguilar 2005; Jang-Condell 2015). For PD0_0, PD45_0, and PD45_45, the disc mass is set to equal the primary disc mass, $0.001\,\mathrm{M_\odot}$. For PD45_0_light, we decrease the perturber disc mass by a factor of 10, such that $m_\mathrm{disc,0} = 10^{-4}\,\mathrm{M_\odot}$. We consider two fly-by orbits tilted by 0° and 45°. For the 45°-inclined orbit, we consider three simulations, PD45_0, PD45_0_light, and PD45_45, where the disc is tilted by 0° (misaligned to the fly-by orbit) and 45° (coplanar to the fly-by orbit), respectively. For PD0_0, PD45_0, and PD45_45, the initial number of SPH particles is set to 10^6, with 500 000 particles within the primary disc and 500 000 particles within the perturber disc. The primary and secondary discs have a shell-averaged smoothing length per scale height of $\langle h \rangle/H \approx 0.5$. For PD45_0_light, the initial number of SPH particles is set to 10^6, with 90 000 particles within the primary disc and 100 000 particles within the perturber disc. The primary has a shell-averaged smoothing length per scale height of $\langle h \rangle/H \approx 0.4$, while the secondary disc has $\langle h \rangle/H \approx 0.8$. The summary of the perturber disc simulations is given in Table 3.

2.3.4 *Analysis routine*

To analyse the hydrodynamical simulations, we average over all particles bound to either the central star or the fly-by. For a particle to be bound to a particular sink, the specific energies (kinetic plus potential) of the particles are negative, neglecting the thermal energy. For each disc, we calculate the mean properties of the particles, such as the surface density, inclination (tilt), longitude of ascending node (twist), eccentricity, and mass. Similar to the N-body simulations, the tilt is measured with respect to the z-axis. We set the time $t = 0$ to represent the time of periastron passage; therefore, the initial time of the simulations will be negative.

2.4 Limitations

In the context of protoplanetary discs, N-body simulations primarily focus on the gravitational interactions between massive bodies and test particles. However, they do not encompass the additional physics that take place within the disc. For instance, N-body simulations are indicative of a collisionless system devoid of pressure/temperature gradients and viscosity – elements that are inherent in protoplanetary discs. While N-body simulations offer valuable insights into the gravitational interactions and overall dynamics of protoplanetary discs, they should be complemented with more intricate models, such as hydrodynamical simulations, that incorporate these supplementary physics (i.e. pressure, temperature gradients, and viscosity). Even a pressure-less fluid would still behave inherently different to N-body dynamics due to the density/velocity fields being multivalued. Hydrodynamical simulations are vital for obtaining a comprehensive understanding of the intricate processes that mold protoplanetary discs during fly-by encounters. It is noteworthy, however, that our hydrodynamical simulations still possess certain limitations, notably pertaining to resolution, a topic discussed in Appendix A. Furthermore, in hydrosimulations of stellar fly-bys with discs it is also important to account for radiation effects – especially for disc-penetrating encounters (as in live radiative calculations by Borchert et al. 2022a, b). These effects are expected to modify the stellar accretion, the three-dimensional-temperature field, and the disc aspect ratio during the encounter. However, the orbital plane of the captured material for disc-grazing encounters (relevant for this work) is expected to remain unchanged. The presence of gas unavoidably damps orbital oscillations that would survive in pure N-body simulations.

3 *N*-BODY RESULTS

Here, we analyse the mass transfer during a parabolic encounter using N-body numerical simulations. Previous works have simulated the interaction between a particle disc and a fly-by with N-body calculations (e.g. Clarke & Pringle 1993; Hall, Clarke & Pringle 1996; Larwood & Kalas 2001; Pfalzner et al. 2005a; Jílková et al. 2016). In particular, Jílková et al. (2016) found that the perturber tilt affected the captured particles' tilt distribution. However, they did not detail the relationship between the captured particles' tilt and the fly-by's initial tilt. We further analyse this by conducting N-body simulations with various initial tilts of the perturber using REBOUND.

Fig. 2 shows the inclination distribution of particles captured by the fly-by. We simulate different initial tilts of the perturber, $i_2 = 0°$, $15°$, $30°$, $45°$, and $60°$. For the coplanar encounter, $i_2 = 0°$, the particles are captured with a coplanar tilt. For each inclined case, the resulting captured particles have an inclination distribution approximately twice the initial perturber tilt. To clarify this, we plot a horizontal dashed line at twice the initial perturber tilt for each case. For example, for $i_2 = 45°$, the captured particles have tilts that are $\sim 90°$ with respect to the tilt of the primary disc. For $i_2 = 60°$, fewer particles are captured, but the captured particles have tilts that are $\sim 120°$, which are considered retrograde orbits. In general, we find as the tilt of the perturber increases, fewer particles are captured. Thus, lower inclination encounters are more efficient at capturing material. This is consistent with the results presented in Jílková et al. (2016). Fig. 3 shows the orbits of the material captured around the fly-by after periastron passage. The inclinations shown in this plot are the same as the ones shown in Fig. 2.

4 HYDRODYNAMICAL RESULTS

4.1 Coplanar prograde fly-by

We first consider a fly-by on a coplanar parabolic orbit (model H0 from Table 2). Fig. 4 shows the evolution of this simulation, where the top row shows the interaction between the coplanar perturber and the primary disc, and the bottom row shows a zoomed-in view centred on the perturber. The second column displays the disc structure when the perturber is at the periastron. At this point, the perturber captures material from the primary disc as gaseous streams. The streams flow around the perturber, forming a disc (seen clearly in the zoomed-in panel). The third and fourth columns display the structure of the two protoplanetary discs shortly after the periastron passage. At these times, a gaseous stream still supports the growth of the forming disc around the perturber.

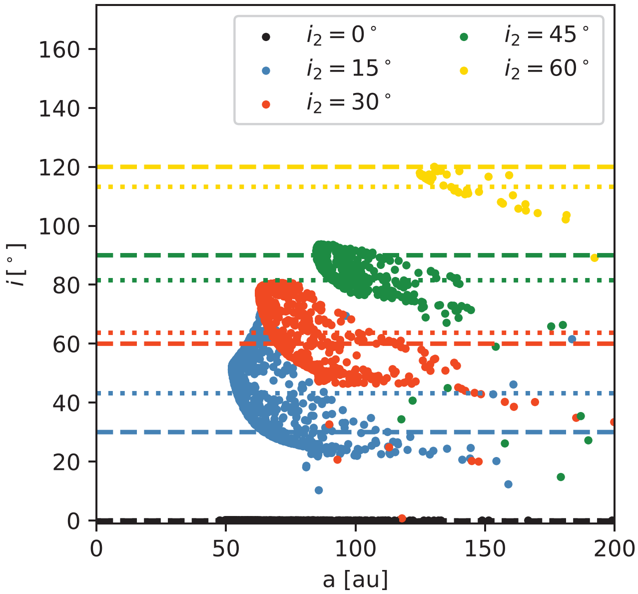

Figure 2. The inclination distribution of particles captured by a parabolic fly-by during our N-body simulations. We compare the distributions for different initial tilt of the fly-by: $i_2 = 0°$ (black, model N0), $15°$ (blue, N15), $30°$ (red, N30), $45°$ (green, N45), and $60°$ (yellow, N60). The horizontal-dotted lines represent the average inclination value for each model. The horizontal-dashed lines denote twice the initial perturber tilt. The particles from each simulation tend to be captured with an inclination roughly twice that of the initial perturber's tilt.

We now investigate the structure of the perturber disc in more detail. The upper panel in Fig. 5 shows the tilt evolution for the primary and perturber discs. The primary disc tilt is initially coplanar and maintains a coplanar profile during and after the encounter. During periastron passage, a disc forms around the perturber that initially forms at a tilt of $\sim 5°$, but then quickly damps to a coplanar orientation, consistent with the N-body simulations. The bottom panel in Fig. 5 shows the ratio of the perturber disc mass to the initial primary disc mass. Shortly after periastron passage, the perturber disc is at peak mass, which is about 10 per cent of the primary disc mass. The secondary disc's mass decreases over time from material accreting on to the perturber.

4.2 45°-inclined fly-by

In this section, we progress from a simplified coplanar encounter to a more probable inclined encounter. Perfectly coplanar/aligned fly-bys are less likely than inclined ones, which can be either prograde or retrograde. Fig. 6 shows the evolution of simulation H45 (a fly-by tilted by 45°). The perturber captures material that forms a disc. However, in this case the disc appears perpendicular to the primary

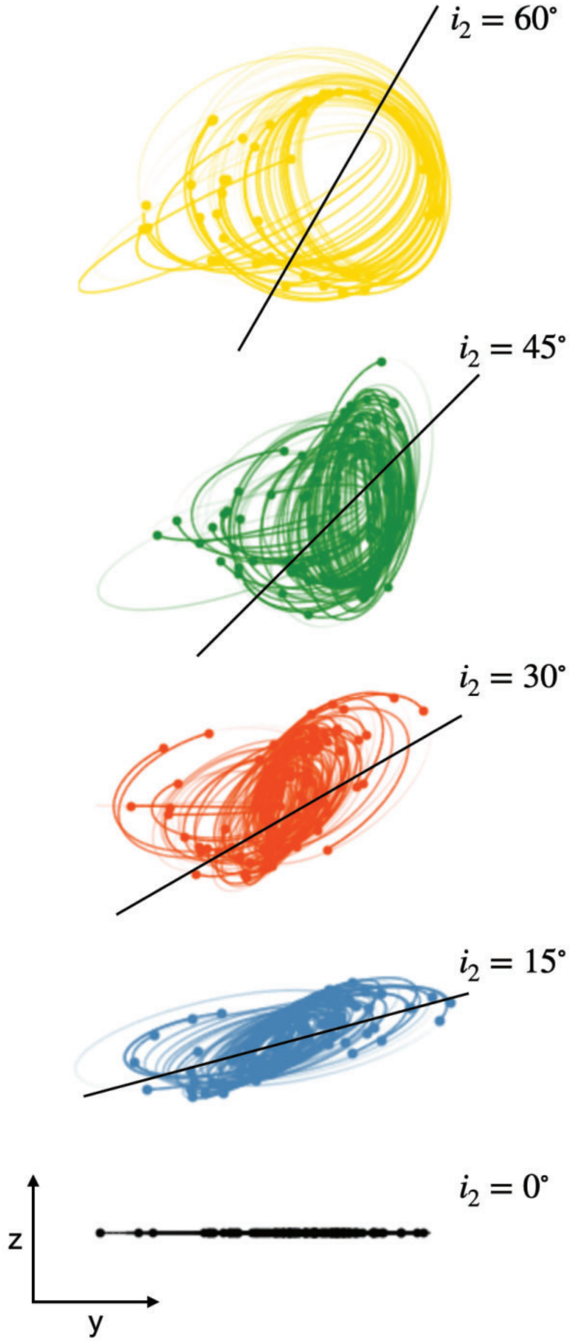

Figure 3. The orbits of captured particles around fly-bys with different initial tilts: $i_2 = 0°$ (black, model N0), 15° (blue, N15), 30° (red, N30), 45° (green, N45), and 60° (yellow, N60). The tilt of the fly-by is represented by the solid black line. The solid dots denote the current position of the particles. We view the orbits in the y–z plane. As the tilt of the perturber increases, the orbits of the majority of captured particles will have an inclination close to twice the initial perturber tilt.

disc in the x–y plane. A resolution study for this specific simulation is given in Appendix A.

The upper panel in Fig. 7 shows the tilt evolution for the primary and perturber discs. The primary disc tilt is initially coplanar but increases to $\sim 4°$ as a consequence of the fly-by encounter. The primary disc maintains this increased tilt for the duration of the simulation. The periastron passage of the fly-by occurs at ~ 2400 yr. At this time, a disc forms around the perturber with an initial tilt of $\sim 98°$, but damps to $\sim 90°$, which is twice the tilt of the perturber (given by the dotted-horizontal line). Therefore, the secondary disc does not form at the same tilt as the perturber orbit but forms a factor of two larger. This is consistent with our *N*-body simulations (see Section 3). Moreover, the mutual inclination between the primary and secondary discs is $\sim 90°$. The bottom panel in Fig. 7 shows the ratio of the perturber disc mass to the primary disc mass. Shortly after periastron passage, the perturber disc grows to peak mass, which is about 3 per cent of the primary disc mass, then decreases over time from material accreting on to the perturber.

Fig. 8 shows the surface density evolution of the disc around the fly-by. At the end of the simulation, the spatial size of the disc extends from ~ 5 to ~ 30 au, with the peak of the surface density profile located at ~ 12 au. The surface density profile goes as $\Sigma \propto r^{-3/2}$. From Fig. 7, we measure the density-weighted average of the disc tilt. We check to see whether the average disc tilt calculated encompasses the entire spatial size of the disc. Fig. 9 shows the tilt evolution as a function of disc radius (x-axis) and time (y-axis). At $t \lesssim 1000$ yr, the tilt of the disc is dominated by material accreting on to the disc at a lower tilt, while at $1000 \text{ yr} \lesssim t \lesssim 2500$ yr the tilt is dominated by material accreting on to the disc at a higher tilt. Beyond ~ 3000 yr after the periastron passage, the disc has a tilt of twice the initial perturber tilt at all radii. In Fig. 10, we take a closer look at the infall on to the circumsecondary disc around the fly-by. There are three streams of material accreting on to the disc. At this time, the more predominant streamer is accreting material at a higher inclination than the other two less predominant streamers.

4.3 Varying fly-by parameters

In this subsection, we vary the tilt, position angle, periastron distance, and mass of the fly-by to explore the robustness of the fly-by disc forming at a tilt twice the initial fly-by tilt, in the latter three experiments we keep the tilt at 45°. Our primary focus centres on quantifying the tilt of the disc. However, to provide a comprehensive analysis, we have also included an examination of the resulting disc phase angle in Appendix B for all simulations.

4.3.1 Fly-by tilt

We analyse how the initial fly-by tilt affects the tilt of the forming disc around the fly-by. The initial fly-by tilts are $i_0 = 0°$, 15°, 30°, 45°, and 60°. The top-left panel in Fig. 11 shows the tilt and mass of the disc around the fly-by as a function of time. The horizontal dotted lines represent twice the initial perturber tilt for initial tilts $i_2 = 0°$–$60°$. When the perturber orbital tilt is 60°, the disc forms retrograde at $\sim 120°$. For this model, we only analyse the disc up to 7000 yr due to low disc resolution because of less material captured by the perturber. The mass of the perturber disc decreases with increasing fly-by tilt, with the coplanar fly-by resulting in the highest disc mass. There is also a delay in the time of peak perturber disc mass and the time of periastron passage, which is shorter as the tilt of the perturber decreases. By varying the fly-by tilt, the forming disc around the perturber still forms at a tilt twice the perturber tilt.

4.3.2 Fly-by position angle

Next, we vary the position angle of the fly-by orbit. We consider position values $\text{PA}_2 = 0°$, 30°, 60°, and 90°. The top-right panel in

Table 2. The set-up of the SPH simulations. The simulation ID is given in the first column. The remaining columns list the mass of the perturber, M_2, the distance of closest approach, $r_{\rm p}$, the initial tilt of the fly-by orbit, i_2, the position angle of the fly-by orbit, PA$_2$, the number of particles, and the tilt of the perturber disc, $i_{\rm disc,\,2}$, along with the standard error.

Simulation ID	M_2 (M$_\odot$)	e_2	$r_{\rm p}$ (au)	i_2 (°)	PA$_2$ (°)	# of particles	$i_{\rm disc,\,2}$ (°)
H0	0.2	1	100	0	0	5×10^5	$\sim$0 ± 0.008
H45	0.2	1	100	45	0	5×10^5	$\sim$90 ± 0.073
H15	0.2	1	100	15	0	5×10^5	$\sim$30 ± 0.066
H30	0.2	1	100	30	0	5×10^5	$\sim$60 ± 0.060
H45HR	0.2	1	100	45	0	4×10^6	$\sim$90 ± 0.041
H60	0.2	1	100	60	0	5×10^5	$\sim$120 ± 0.098
H45PA30	0.2	1	100	45	30	5×10^5	$\sim$90 ± 0.032
H45PA60	0.2	1	100	45	60	5×10^5	$\sim$90 ± 1.634
H45PA90	0.2	1	100	45	90	5×10^5	$\sim$90 ± 1.850
H45R120	0.2	1	120	45	0	5×10^5	$\sim$90 ± 0.040
H45R80	0.2	1	80	45	0	5×10^5	$\sim$90 ± 0.029
H45M1	1	1	100	45	0	5×10^5	$\sim$90 ± 0.039
H45p3	0.2	0.3	100	45	0	5×10^5	$\sim$92 ± 0.164
H45p5	0.2	0.7	100	45	0	5×10^5	$\sim$90 ± 0.492

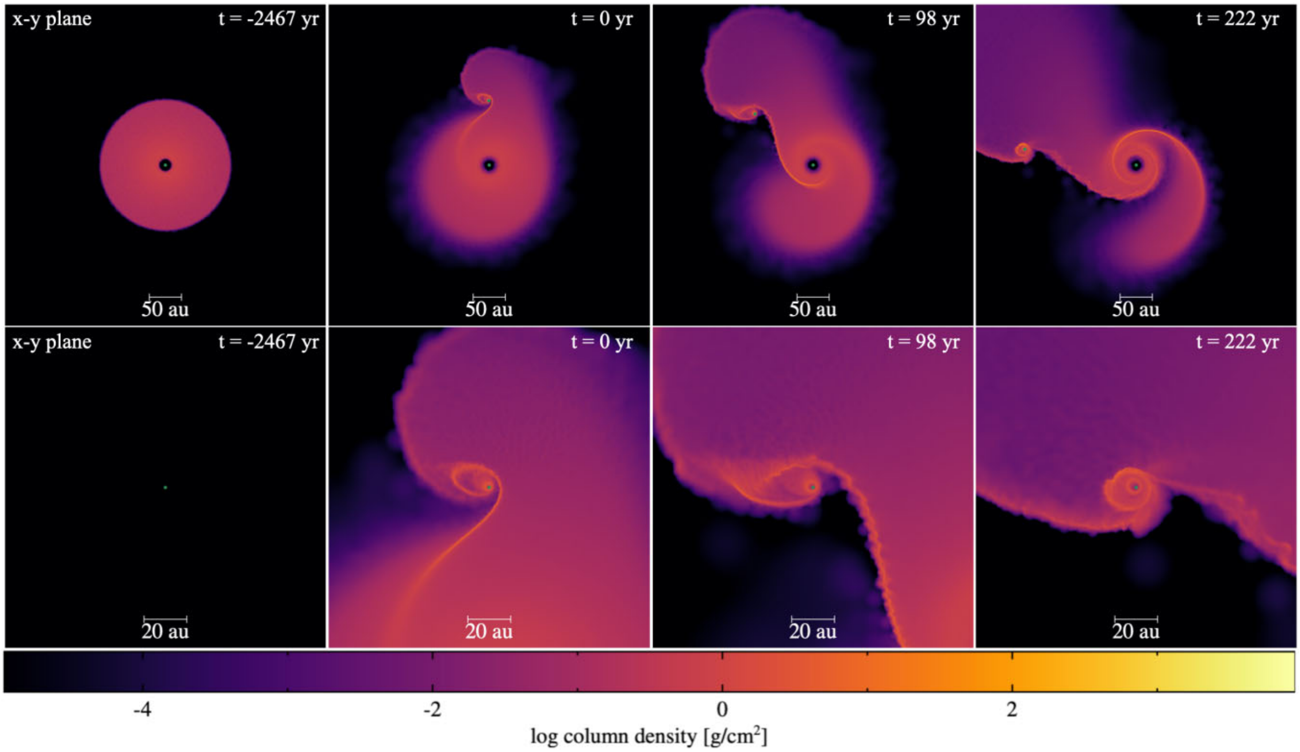

Figure 4. The evolution and formation of protoplanetary discs around the primary star and perturber (green dots) during a coplanar prograde encounter (model H0). The frames in the top row are centred on the primary star, while the frames in the bottom row are zoomed-in and centred on the fly-by. All the frames are viewed in the x–y plane, which is face-on to the primary disc. The first column shows the primary disc and perturber at the beginning of the simulation. The second column shows the disc structure during the periastron passage of the fly-by ($t = 0$ yr). The third and fourth columns represent times shortly after the periastron passage, indicating the formation of the disc around the fly-by. The colour denotes the disc surface density.

Fig. 11 shows the perturber disc tilt and mass as a function of time for the different position angle models. The horizontal dotted line represents twice the initial perturber tilt of 45°. The perturber disc is captured at a tilt of $\sim$90° regardless of the position angle of the fly-by. A PA$_2 = 0°$ fly-by results in the highest disc mass out of all the PA simulations. When PA$_2 = 30°$ and 60°, the disc mass is similar with a mass of $\sim$1 per cent of the primary disc mass. For PA$_2 = 90°$, the disc mass is $\sim$2 per cent of the primary disc mass. This is because when PA$_2 = 90°$, the fly-by has two closest approaches on either side of the primary disc, capturing more material. By varying the fly-by position angle, the forming disc around the perturber still forms at a tilt twice the perturber tilt.

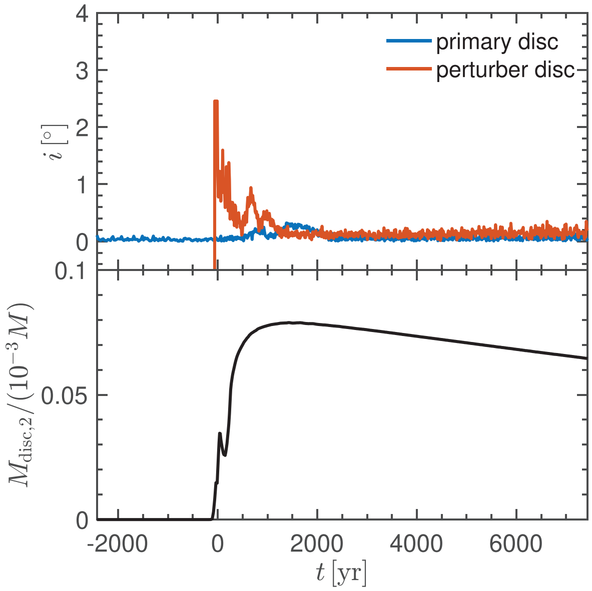

Figure 5. Top panel: The tilt of the primary disc (blue) and perturber disc (red) for a coplanar perturber (model H0). Bottom panel: The fraction of the perturber disc mass to the initial primary disc mass. The captured material around the perturber is nearly in a coplanar orientation.

4.3.3 Fly-by periastron

Next, we vary the periastron distance of the fly-by orbit. We consider position values $r_{\rm p} = 80$, 100, and 120 au. The bottom-left panel in Fig. 11 shows the perturber disc tilt and mass as a function of time for the different periastron distance models. The horizontal dotted line represents twice the initial perturber tilt of 45°. For periastron distances, $r_{\rm p} = 80$, 100, and 120 au, the tilt of the perturber disc is 90° (twice the initial perturber tilt) with respect to the z-axis. For $r_{\rm p} = 80$ au, the perturber penetrates the disc, resulting in the highest disc mass compared to the periastron distance simulations. Moreover, as the periastron distance of the perturber increases, the resulting disc mass decreases. By varying the fly-by periastron distance, whether a grazing or lightly penetrating encounter, the forming disc around the perturber still forms at a tilt twice the perturber tilt.

4.3.4 Fly-by mass

Finally, we vary the mass of the fly-by. We consider mass values of $M_2 = 0.2$ and 1 $\mathrm{M}_\odot$. The bottom-right panel in Fig. 11 shows the perturber disc tilt and mass as a function of time for the different fly-by mass models. The horizontal dotted line represents twice the initial perturber tilt of 45°. For $M_2 = 0.2$ and 1 $\mathrm{M}_\odot$, the disc forming around the perturber has a tilt slightly larger than twice the perturber tilt. The more massive perturber captures more material, resulting in a higher disc mass of ∼10 per cent of the primary disc mass. We can see that varying the fly-by mass does have a small affect on the final disc inclination, but the disc that forms still has roughly twice the initial perturber tilt.

5 INTERACTING PROTOPLANETARY DISCS

This section explores situations where the perturber initially has a protoplanetary disc before interacting with the primary disc. We simulate three combinations of the perturber and disc around the perturber (given in Table 3) that are (1) a coplanar fly-by with a disc coplanar to the fly-by orbit, (2) a 45°-inclined fly-by with a disc coplanar to the primary disc, and (3) a 45°-inclined fly-by, with a disc coplanar to the fly-by orbit. Fig. 12 shows the disc surface density for the two interacting protoplanetary discs for a 45°-inclined fly-by, with a 45°-tilted disc (model PD45_45). The top row is centred on the primary disc, and the bottom row is centred on the disc around the perturber. The first column represents the initial structure of the two discs. The second column shows the time of periastron passage of the perturber. The two discs interact with one another, where material from the secondary disc is transferred to the primary and vice versa. The third and fourth columns show times shortly after the periastron passage. Gaseous streams from the primary disc are accreting on to the perturber disc.

Next, we look at the change in the tilt of the perturber disc after interacting with the primary disc. Fig. 13 shows the tilt profile as a function of time for the four models of interacting protoplanetary discs, PD0_0 (blue), PD45_0 (red), PD45_0_light (yellow), and PD45_45 (purple). During a coplanar interaction (PD0_0), the secondary disc remains coplanar after interacting with the primary disc. For an inclined fly-by with a coplanar disc (PD45_0), the coplanar disc increases to a tilt of ∼10° after interacting with the primary disc. For an inclined fly-by with a coplanar low-mass disc (PD45_0_light) increases to a tilt of ∼30° after interacting with the primary disc. Lastly, for an inclined fly-by with a 45°-tilted disc (PD45_45), the tilt of the secondary disc increases a small amount to ∼47°. Unlike the simulations without an initial secondary disc, there is no straightforward relationship between the perturber orbital tilt and the secondary disc tilt. This result is strongly dependent on the balance of the initial fly-by disc angular momentum to the angular momentum of captured particles. The simulations described above have an initial circumsecondary disc around the fly-by with an angular momentum equal to the primary disc. If the angular momentum of the fly-by disc is significantly less than the angular momentum of the captured particles, the disc around the fly-by should form at a different tilt than the original tilt.

6 WHY A FACTOR OF TWO?

Both our N-body and SPH calculations have motivated that the captured material has an inclination twice that of the encounter. Importantly, this result appears robust to changes in the mass of the perturber, the inclination of the encounter, the distance of closest approach, and the position angle of the fly-by. Here, we will provide an analytic framework for this behaviour that is informed by our previous simulations.

The step-function nature of the inclination in Fig. 7 demonstrates that the inclination of the gas does not appreciably change after the interaction. That is, the angular momentum of the material that finishes around the perturber is what it has *at the instant* it is captured during the pericentre passage. We can thus calculate the properties of the gas while it is in the disc and safely assume that those properties will broadly hold as the captured material is carried away by the perturber. As the relative orientation of the gas is determined by its angular momentum, we will focus on a description of this here.

First, we consider the gas in the primary disc. From the primary star, the distance to a particular region of the disc is given by $\boldsymbol{r}_1$, where

$$\boldsymbol{r}_1 = (r_1 \cos\phi, r_1 \sin\phi, 0), \tag{10}$$

and ϕ is the angle measured from the point of closest approach between the perturber and primary star (see the left panel in Fig. 1).

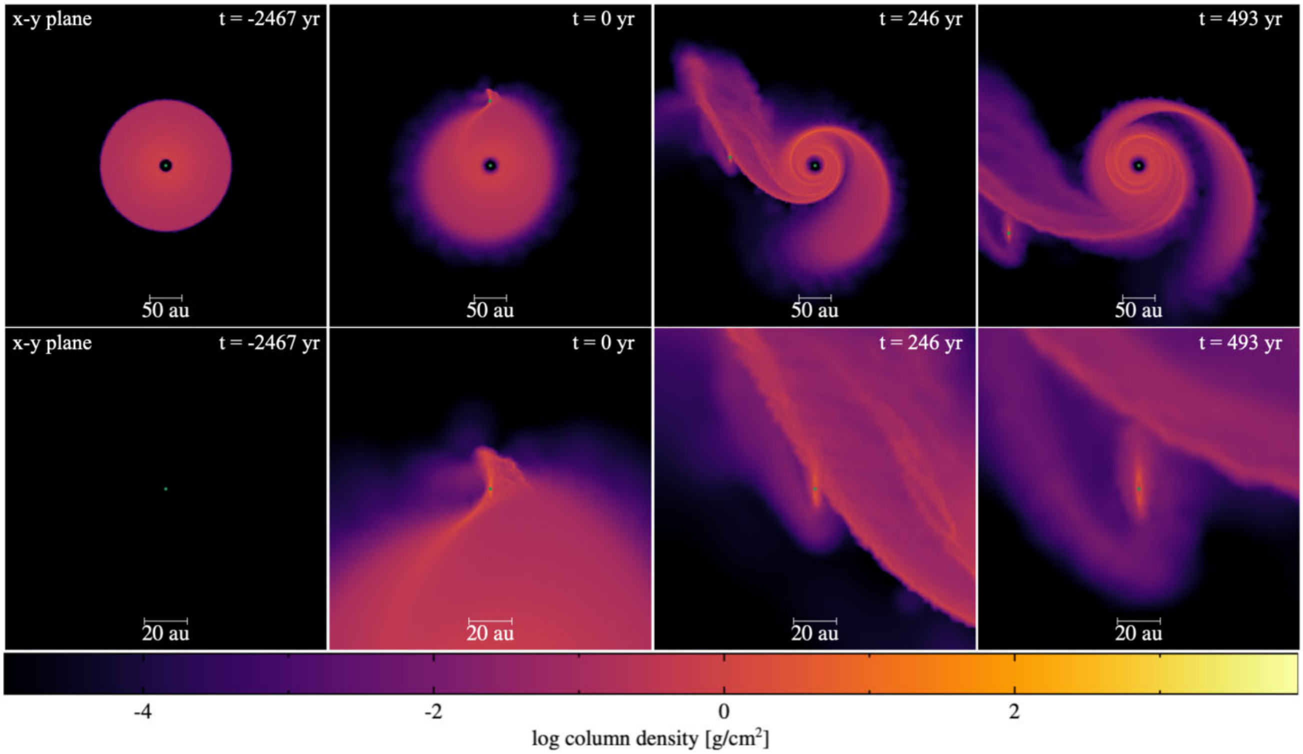

Figure 6. Same as Fig. 4 but for a 45° inclined perturber (model H45).

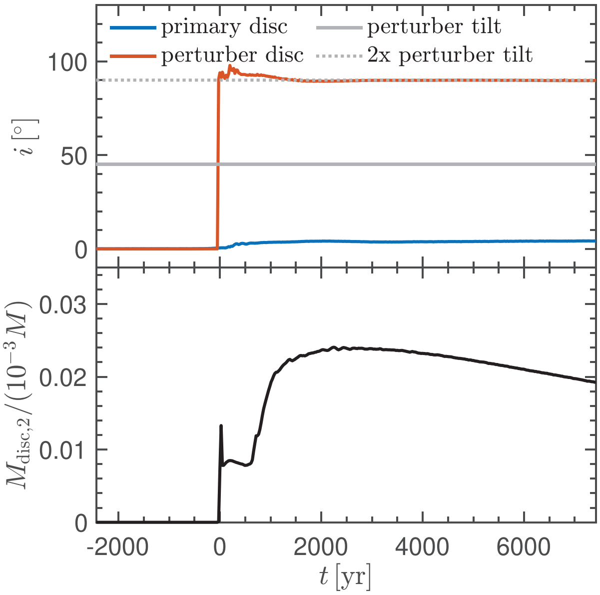

Figure 7. Same as Fig. 5 but for a 45° inclined perturber (model H45). The tilt of the perturber is shown by the horizontal grey line, and twice the perturber tilt is shown by the horizontal dotted grey line.

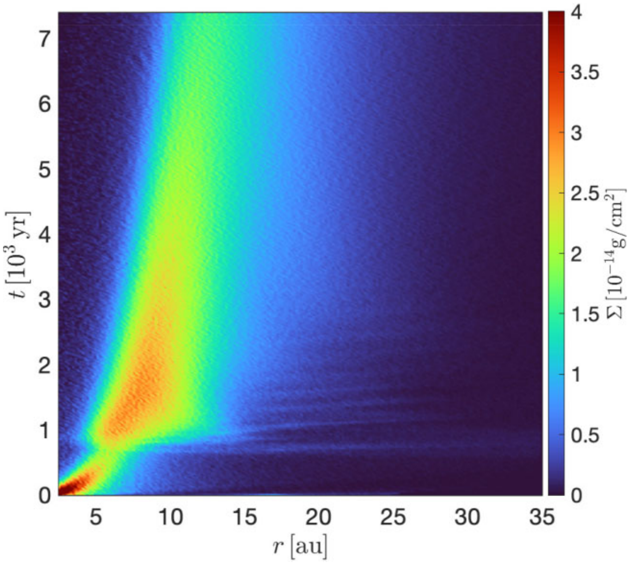

Figure 8. The surface density evolution for the second-generation disc. The x-axis shows the disc radius, while the y-axis shows the time with $t = 0$ yr being the time of periastron passage. The colour denotes the surface density.

If the disc is otherwise undisturbed the material will have a Keplerian rotation profile given by

$$\boldsymbol{v}_1 = (-v_{\rm Kep}\sin\phi,\, v_{\rm Kep}\cos\phi,\, 0), \tag{11}$$

with $v_{\rm Kep} = \sqrt{GM_1/r_1}$. Second, we consider the motion of the perturber. Our perturber approaches on an inclined path defined by the angle i_0, measured from the mid-plane of the primary disc. The path of the perturber with respect to the primary is then described as (e.g. D'Onghia et al. 2010)

$$\boldsymbol{r}_2 = (-r_2\cos i_0\sin i_0,\, r_2\cos i_0,\, r_2\sin i_0\sin i_0). \tag{12}$$

Similarly, the perturber has a velocity given by

$$\boldsymbol{v}_2 = (-v_0\cos i_0,\, 0,\, v_0\sin i_0), \tag{13}$$

with $v_0 = \sqrt{2G(M_1 + M_2)/r_{\rm p}}$, where $r_{\rm p}$ is the closest approach distance. During the encounter, the perturber imparts an impulse to

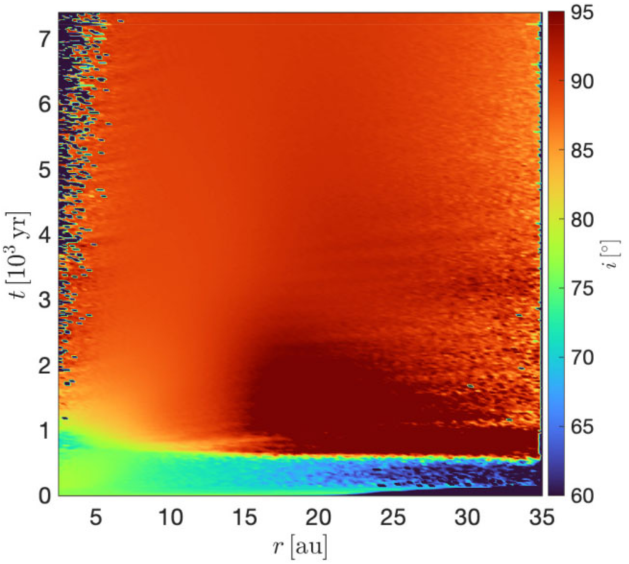

Figure 9. The tilt evolution for the second-generation disc. The x-axis shows the disc radius, while the y-axis shows the time with $t = 0$ yr being the time of periastron passage. The colour denotes the tilt.

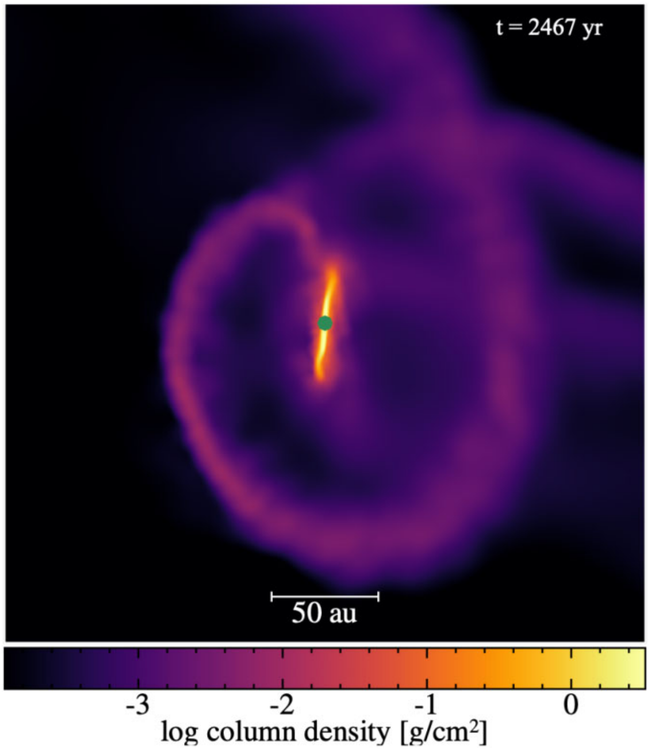

Figure 10. The formation of second-generation disc around the perturber (green dot) during a 45°-inclined fly-by (model H45). Multiple gaseous streamers are present with the more prominent streamer accreting material at a higher inclination than the less prominent streamers.

the gas in the disc which we name $\Delta \boldsymbol{v}$. We follow the method outlined in D'Onghia et al. (2010) to calculate this velocity perturbation driven by an inclined, parabolic fly-by. We refer the interested reader to Appendix C for the full form of $\Delta \boldsymbol{v}$.

Finally, we consider the velocity and position of the gas in the disc with respect to the perturber. Straightforwardly,

$$\boldsymbol{R} = \boldsymbol{r}_1 - \boldsymbol{r}_2, \tag{14}$$

and

$$\boldsymbol{V} = \boldsymbol{v}_1 + \Delta \boldsymbol{v} - \boldsymbol{v}_2. \tag{15}$$

We find for the parameters chosen in our problem $|\Delta \boldsymbol{v}| \ll |\boldsymbol{V}|$ for all typical combinations of the perturber properties (inclination, mass, pericentre distance, position angle, etc.). This suggests that the velocity of the gas in the disc as measured from the perturber is effectively only dependent on perturber properties; the mass of the primary, the total mass of the stars, the inclination of the encounter and the distance of closest approach. We can thus use equations (14) and 15 to calculate the angular momentum of the gas with respect to the perturber and as a result, measure the inclination of the material with respect to the perturber.

From these two expressions we can calculate the angular momentum of the gas, $\boldsymbol{L}_2 = m(\boldsymbol{R} \times \boldsymbol{V})$ averaged across each particle bound to the perturber, at any point during the encounter. The upper panels of Fig. 14 show this for the fiducial calculation with $i_0 = 45^\circ$. Measured from the frame of the perturber, the inclination of the gas varies between 0° and ∼120° with higher inclinations on the side closest to the perturber.

In the lower panels of Fig. 14, we show the inclination of the gas that is captured at each snapshot. By only highlighting these particles it is clear that the inclination of the captured material *at the instance of capture* is ∼70°–90°. More importantly, as the simulation evolves the region where particles are able to be captured from moves such that material with roughly the same inclination is captured at different time-steps. The serendipitous capture of particles from a region that has roughly twice the inclination of the encounter appears to be the cause of the factor of two identified across all of our simulations.

The capture of this material depends on the relative velocity, so we further test this relationship by conducting additional simulations with different approach speeds. Fig. 15 shows how the inclination of the captured disc around the perturber varies with different eccentricities: $e_2 = 0.3$ (blue, H45p3), 0.7 (red, H45p5), and 1 (yellow, H45). The simulations for the bound cases are conducted for a single orbit, which imitates a fly-by scenario. The three curves are indistinguishable up to their individual cut-off points. While the relative velocity between the primary disc and perturber is responsible for determining the factor of two in inclination, we find that even a large change in the energy of the encounter produces only a small change in the relative inclination.

7 DISCUSSION

Our results demonstrate that the relative inclination between the two discs after a fly-by encounter can reveal the initial inclination of the encounter, as long as the perturber did not have a disc initially. Here, we consider what that means for existing observations of fly-bys. Observational evidence of a fly-by encounter includes: (1) tidally induced spirals, (2) long bridges of material connecting to the perturber, and (3) formation of second-generation discs. Several systems with protoplanetary discs being perturbed by a fly-by candidate are currently observed (e.g. Cuello et al. 2023). The relationship between the disc inclination and the perturber during a fly-by encounter is independent of the perturber's mass, periastron distance, or position angle. If a fly-by system is identified to have a second-generation disc around the fly-by, these steps can be used to reconstruct the tilt of the fly-by during the encounter:

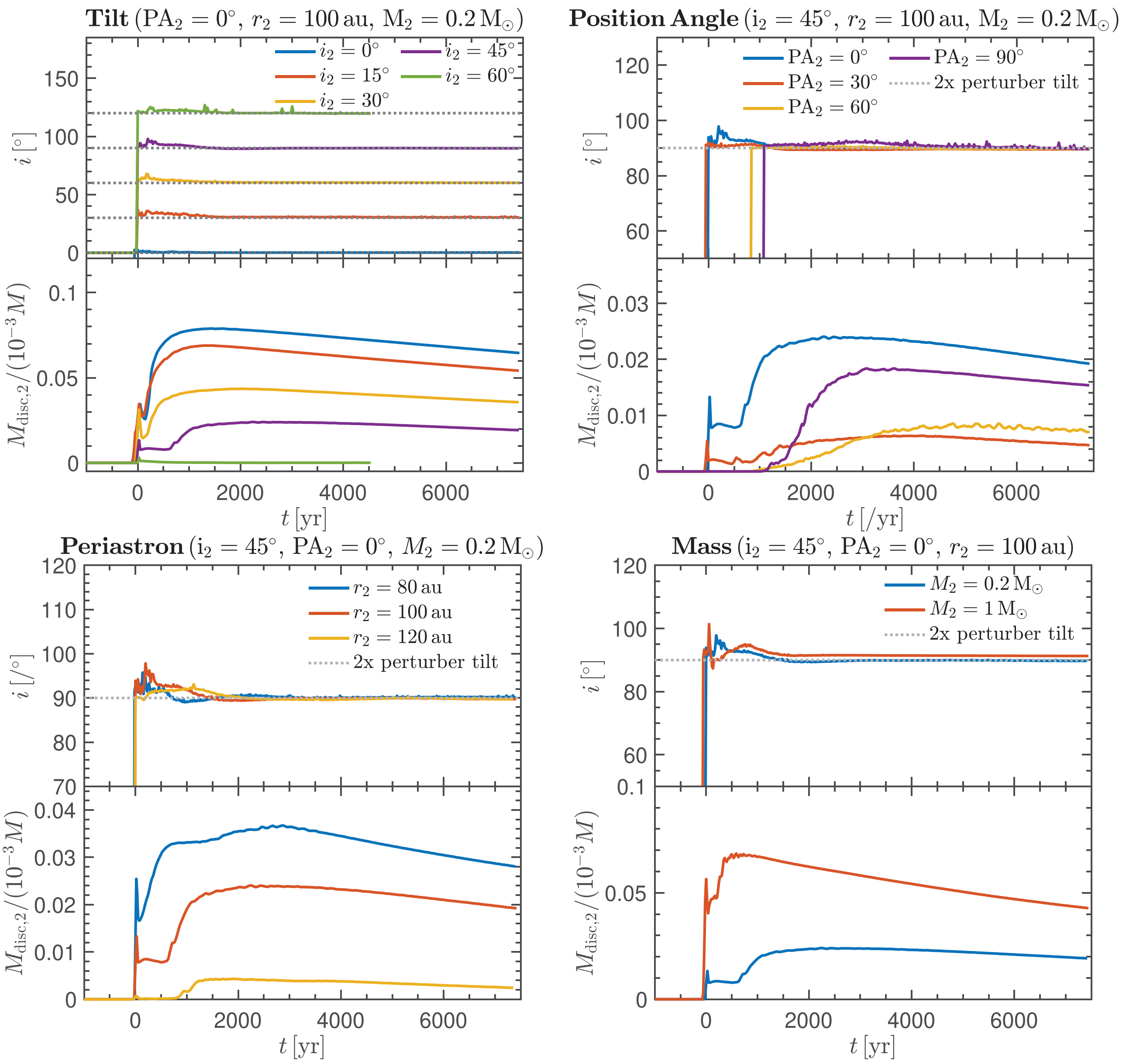

Figure 11. The evolution of the tilt and mass of the disc forming around the perturber for different parameters of the perturber: tilt (top-left panel), position angle (top-right panel), periastron distance (bottom-left panel), and mass (bottom-right panel). For the position angle, periastron distance, and mass, the fly-by orbit is set to 45°. The horizontal lines show twice the initial tilt of the respected fly-by orbits. The analysis of the disc around the 60°-inclined perturber due to low disc resolution from the lower amount of captured material. In each case, the forming disc around the fly-by is captured at twice the initial perturber tilt.

Table 3. The set-up of the SPH simulations with an initial disc around the perturber. The simulation ID is given in the first column. The remaining columns list the tilt of the fly-by orbit, i_2, initial tilt of the perturber disc, $i_{\rm disc,\,0}$, the initial mass of the perturber disc, $m_{\rm disc,\,0}$, and the final tilt of the perturber disc $i_{\rm disc,\,2}$, along with the standard error.

Simulation	i_2 (°)	$i_{\rm disc,\,0}$ (°)	$m_{\rm disc,\,0}$ (M$_\odot$)	$i_{\rm disc,\,2}$ (°)
PD0_0	0	0	0.001	∼0 ± 0.005
PD45_0	45	0	0.001	∼10 ± 0.078
PD45_0_light	45	0	0.0001	∼30 ± 0.072
PD45_45	45	45	0.001	∼47 ± 0.012

(i) Measure the mutual inclination between the primary disc and the disc around the fly-by candidate.

(ii) If the disc formed during the encounter, its tilt will be roughly twice the initial tilt of the fly-by orbit.

(iii) Estimate the tilt of the fly-by orbit based on this relationship.

The most compelling case to test the relationship between disc inclination and perturber tilt is the system UX Tau. UX Tau is a young quadruple system, located in the Taurus star-forming region. The circumstellar disc around UX Tau A and UX Tac C shows signs of dynamical interaction, where the large spirals are detected in the disc around UX Tau A and a long bridge of material extends between

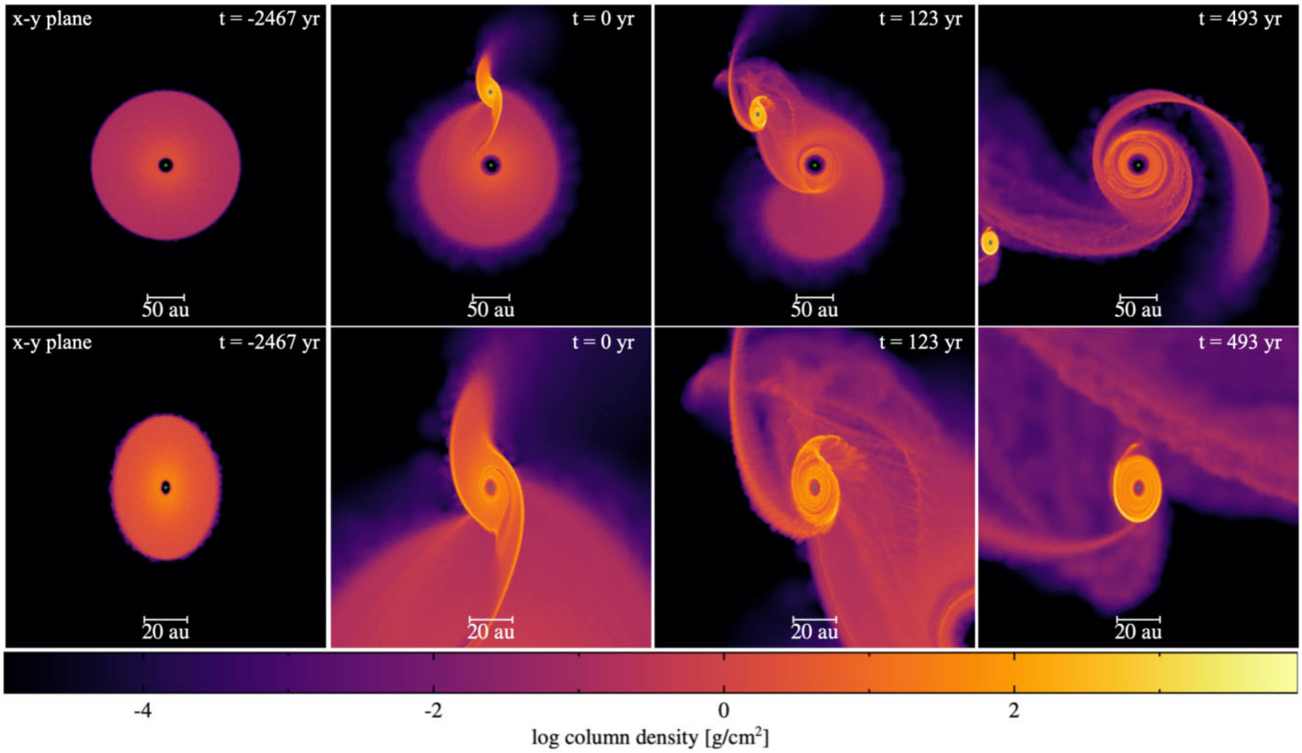

Figure 12. The evolution of two interacting protoplanetary discs around the primary star and perturber (green dots) during a coplanar prograde encounter (model PD45_45). The frames in the top row are centred on the primary star, while the frames in the bottom row are zoomed-in and centred on the fly-by. All the frames are viewed in the x–y plane, which is face-on to the primary disc. The first column shows the primary disc and perturber at $t = 0$ yr. The second column shows the disc structure during the periastron passage of the fly-by. The third and fourth columns represent times shortly after the periastron passage, indicating the formation of the disc around the fly-by. The colour denotes the disc surface density.

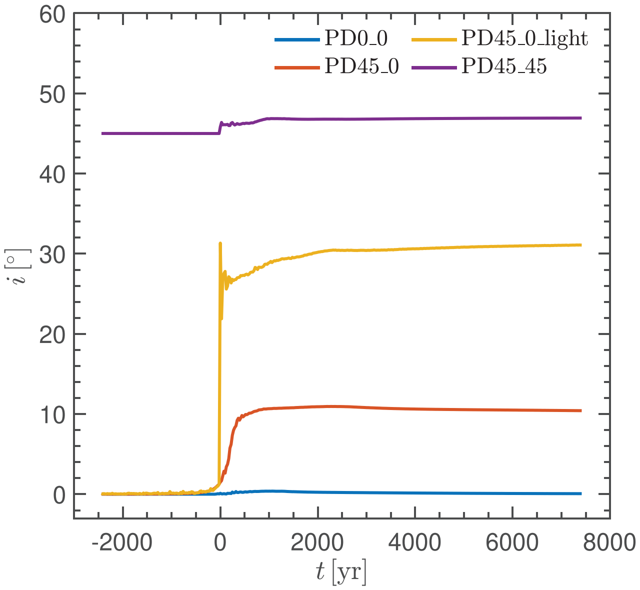

Figure 13. A summary of the perturber disc tilt as a function of time for the four interacting protoplanetary disc simulations. We show the models PD0_0 (blue), PD45_0 (red), PD45_0_light (yellow), and PD45_45 (purple).

UX Tau A and UX Tau C. The rotational signature of the two discs can be clearly seen in the map of the peak intensity velocity (e.g. Ménard et al. 2020). From the observations, the two discs have a mutual inclination of ~80° (e.g. Francis & van der Marel 2020; Ménard et al. 2020). The disc around the fly-by candidate UX Tau C does not show millimetre emission in the disc and the mm-sized dust disc around UX Tau A is more compact than the gas disc. The observations are consistent with the disc around UX Tau C was formed during the fly-by encounter. In such a scenario, we can use the results in this work to reconstruct the initial tilt of UX Tau C to be ~40°.

It is not clear whether the remaining observations of discs around fly-by candidates were formed during the encounter, i.e. a second-generation disc, or if the discs around the perturber were present before the encounter. Observations of SR 24 (also known as HBC 262) show a bridge of material between SR 24N and connecting to the disc around SR 24S (Mayama et al. 2010, 2020; Weber et al. 2023), suggesting a fly-by event has recently occurred. AS 205 is a triple-star system where two components are resolved, AS 205 N and AS 205 S. The discs around each component are misaligned to one another with a bridge of gas between the two sources detected by the ALMA ^{12}CO (J = 2–1) data (Kurtovic et al. 2018) and by SPHERE in scattered light (Weber et al. 2023). From the ALMA observations, the disc around the fly-by candidate, AS 205 S, displays millimetre emission, which suggests the disc was present before the encounter. The gaseous bridge between FU Ori N and FU Ori S is misaligned with respect to the disc mid-plane (Pérez et al. 2020; Weber et al. 2023), which is evidence of an inclined fly-by encounter. An inclined fly-by has also been proposed to explain the disc morphology for two systems, Z CMa (Dong et al. 2022) and Sgr C (Lu et al. 2022). Further observations are needed to identify whether the discs around the perturber are thought to be second generation or present prior to the encounter.

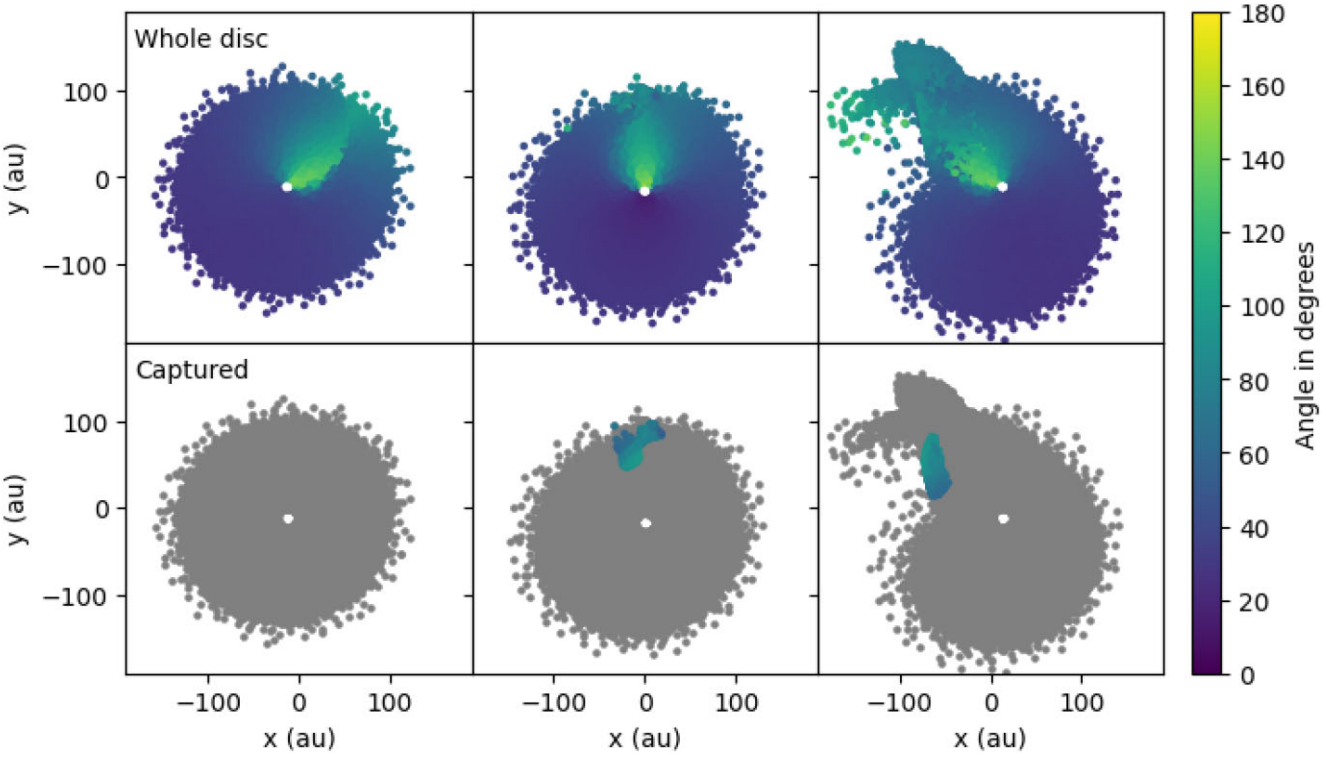

Figure 14. Inclination of the gas in the disc from the frame of the perturber for simulation H45HR. *Upper panel*: Inclination of every particle in the disc assuming it was in orbit around the perturber. *Lower panel*: Only particles captured in this time-step are indicated, showing where these particles come from. The relative inclination of the gas particles varies across the disc and depends on the location of the perturber. Particles captured by the perturber are serendipitously selected from the region that always corresponds to roughly a factor of twice the original inclination.

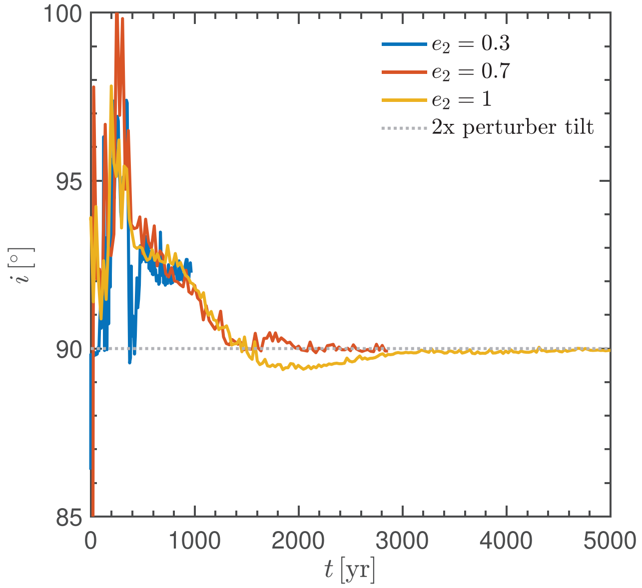

Figure 15. The tilt of the captured disc around the perturber with different eccentricities, $e_2 = 0.3$ (blue, H45p3), 0.7 (red, H45p5), and 1 (yellow, H45). The bound cases are only simulated for one orbit, which imitates a fly-by. Therefore, the dotted lines show the data extrapolated to the simulation end-time of H45. The perturber with eccentricities $e_2 = 0.7$ and 1 form a disc with a tilt twice the initial perturber tilt (grey dotted line). The perturber with a lower eccentricity, $e_2 = 0.3$, forms a disc that is not exactly twice the initial perturber tilt.

8 SUMMARY

We investigated the interaction of a protoplanetary disc with a grazing parabolic orbit fly-by using both *N*-body and three-dimensional SPH simulations. Our simulations and the corresponding analysis were conducted to examine the relationship between the perturber's tilt and the resulting tilt of the second-generation discs. Through systematic variation of the perturber tilt, it was discovered that the tilt of the resulting second-generation discs consistently maintained a proportional relationship, precisely twice that of the perturber.

Through *N*-body simulations, we find a prograde encounter can efficiently capture material when the fly-by's periastron is close to the outer disc edge. The captured material can form a second-generation disc around the fly-by (Clarke & Pringle 1993; Muñoz et al. 2015; Cuello et al. 2019). We investigate the inclination distribution of captured particles based on the initial tilt of the fly-by orbit. We find a relationship where particles are captured with a tilt twice the perturber's initial tilt. This relationship is evident in fig. 20 in Jílková et al. (2016).

We then consider highly resolved hydrodynamical simulations of a fly-by encountering a protoplanetary disc. We find that the captured, second-generation disc forms at a tilt twice the initial fly-by tilt. This relationship holds when we vary the fly-by's tilt, position angle, periastron, and mass. Analysing the disc characteristics, such as eccentricity and tilt, of these second-generation discs can give information about the orbital properties of the fly-by encounter (Jílková et al. 2016). Therefore, knowing the relationship between the tilt of the second-generation disc and the tilt of the fly-by orbit can be used to reconstruct the trajectory of the fly-by provided that there was no disc prior to the encounter. We also simulate the case where the fly-by has a disc of material prior to the encounter, and find that the tilt of the eventual circumsecondary disc after the fly-by is determined by both the initial state of the circumsecondary disc and the fly-by geometry.

The findings in this work carry significant implications for our understanding of disc formation and orbital dynamics. It suggests a robust correlation between the perturber's tilt and the subsequent tilt of second-generation discs, providing valuable insights into the mechanisms governing their formation. Additionally, this observation highlights the importance of considering the relative angular orientations when studying the evolution and characteristics of second-generation discs.

ACKNOWLEDGEMENTS

We would like to thank the referee and editor for their invaluable contributions in enhancing the quality of the manuscript. The authors would like to thank Grant Kennedy and Dimitri Veras for discussions. JLS acknowledges funding from the ASIAA Distinguished Postdoctoral Fellowship. RN acknowledges funding from UKRI/EPSRC through a Stephen Hawking Fellowship (EP/T017287/1). This research was supported by the Munich Institute for Astro-, Particle and BioPhysics (MIAPbP) that is funded by the Deutsche Forschungsgemeinschaft (DFG, German Research Foundation) under Germany's Excellence Strategy – EXC-2094 – 390783311. This research was funded, in part, by ANR (Agence Nationale de la Recherche) of France under contract number ANR-22-ERCS-0002-01. This project has received funding from the European Research Council (ERC) under the European Union Horizon Europe programme (grant agreement no. 101042275, project Stellar-MADE). RD is supported by the Natural Sciences and Engineering Research Council of Canada (NSERC) and the Alfred P. Sloan Foundation. RAB is supported by a Royal Society University Research Fellowship.

DATA AVAILABILITY

The data supporting the plots within this article are available on reasonable request to the corresponding author. The *N*-body integrations in this work made use of the REBOUND code that can be downloaded freely at http://github.com/hannorein/rebound. A public version of the PHANTOM and SPLASH codes are available at https://github.com/danieljprice/phantom and http://users.monash.edu.au/~dprice/splash/download.html, respectively.

REFERENCES

Adams F. C., Proszkow E. M., Fatuzzo M., Myers P. C., 2006, ApJ, 641, 504
Andrews S. M., 2020, ARA&A, 58, 483
Artymowicz P., Lubow S. H., 1994, ApJ, 421, 651
Bate M. R., 2018, MNRAS, 475, 5618
Bate R. R., Mueller D. D., White J. E., 1971, Fundamentals of Astrodynamics, Courier Dover Publications
Beck T. L., Aspin C., 2012, AJ, 143, 55
Bhandare A., Breslau A., Pfalzner S., 2016, A&A, 594, A53
Borchert E. M. A., Price D. J., Pinte C., Cuello N., 2022a, MNRAS, 510, L37
Borchert E. M. A., Price D. J., Pinte C., Cuello N., 2022b, MNRAS, 517, 4436
Breslau A., Vincke K., Pfalzner S., 2017, A&A, 599, A91
Cabrit S., Pety J., Pesenti N., Dougados C., 2006, A&A, 452, 897
Carpenter J. M., 2000, AJ, 120, 3139
Clarke C. J., Pringle J. E., 1993, MNRAS, 261, 190
Concha-Ramírez F., Wilhelm M. J. C., Portegies Zwart S., Haworth T. J., 2019, MNRAS, 490, 5678
Concha-Ramírez F., Wilhelm M. J. C., Portegies Zwart S., van Terwisga S. E., Hacar A., 2021, MNRAS, 501, 1782
Cuello N. et al., 2019, MNRAS, 483, 4114
Cuello N. et al., 2020, MNRAS, 491, 504
Cuello N., Ménard F., Price D. J., 2023, Eur. Phys. J. Plus, 138, 11
D'Onghia E., Vogelsberger M., Faucher-Giguere C.-A., Hernquist L., 2010, ApJ, 725, 353
Dai F., Facchini S., Clarke C. J., Haworth T. J., 2015, MNRAS, 449, 1996
Dai Y.-Z., Liu H.-G., Wu W.-B., Xie J.-W., Yang M., Zhang H., Zhou J.-L., 2018, MNRAS, 480, 4080
Dong R. et al., 2022, Nat. Astron, 6, 331
Farris B. D., Duffell P., MacFadyen A. I., Haiman Z., 2014, ApJ, 783, 134
Francis L., van der Marel N., 2020, ApJ, 892, 111
Garufi A. et al., 2020, A&A, 633, A82
Grady C. A., Woodgate B., Bruhweiler F. C., Boggess A., Plait P., Lindler D. J., Clampin M., Kalas P., 1999, ApJ, 523, L151
Grady C. A. et al., 2013, ApJ, 762, 48
Haisch K. E., Jr, Lada E. A., Lada C. J., 2001, ApJ, 553, L153
Hall S. M., Clarke C. J., Pringle J. E., 1996, MNRAS, 278, 303
Hernández J. et al., 2007, ApJ, 662, 1067
Hernández J., Hartmann L., Calvet N., Jeffries R. D., Gutermuth R., Muzerolle J., Stauffer J., 2008, ApJ, 686, 1195
Hillenbrand L. A., 1997, AJ, 113, 1733
Jang-Condell H., 2015, ApJ, 799, 147
Jílková L., Hamers A. S., Hammer M., Portegies Zwart S., 2016, MNRAS, 457, 4218
Jiménez-Torres J. J., 2020, Acta Astron., 70, 53
Kurtovic N. T. et al., 2018, ApJ, 869, L44
Lada C. J., Lada E. A., 2003, ARA&A, 41, 57
Larwood J. D., Kalas P. G., 2001, MNRAS, 323, 402
Larwood J. D., Papaloizou J. C. B., 1997, MNRAS, 285, 288
Lin D. N. C., Papaloizou J. C. B., 1993, in Levy E. H., Lunine J. I., eds, Protostars and Planets III. p. 749, Univ. Arizona Press Tucson, AZ
Lodato G., Price D. J., 2010, MNRAS, 405, 1212
Lodato G., Pringle J. E., 2007, MNRAS, 381, 1287
Lu X., Li G.-X., Zhang Q., Lin Y., 2022, Nat. Astron., 6, 837
Mamajek E. E., 2009, in Usuda T., Tamura M., Ishii M., eds, AIP Conf. Proc. Vol. 1158, Exoplanets And Disks: Their Formation And Diversity. Am. Inst. Phys., New York, p. 3
Mayama S. et al., 2010, Science, 327, 306
Mayama S. et al., 2020, AJ, 159, 12
Ménard F. et al., 2020, A&A, 639, L1
Meru F., Bate M. R., 2012, MNRAS, 427, 2022
Monaghan J. J., 1989, J. Comput. Phys., 82, 1
Monnier J. D. et al., 2019, ApJ, 872, 122
Muñoz D. J., Kratter K., Vogelsberger M., Hernquist L., Springel V., 2015, MNRAS, 446, 2010
Muro-Arena G. A. et al., 2020, A&A, 636, L4
Muto T. et al., 2012, ApJ, 748, L22
Nealon R., Cuello N., Alexander R., 2020, MNRAS, 491, 4108
Olczak C., Pfalzner S., Spurzem R., 2006, ApJ, 642, 1140
Ostriker E. C., 1994, ApJ, 424, 292
Papaloizou J. C. B., Lin D. N. C., 1995, ApJ, 438, 841
Papaloizou J. C. B., Pringle J. E., 1983, MNRAS, 202, 1181
Pérez S. et al., 2020, ApJ, 889, 59
Pfalzner S., 2003, ApJ, 592, 986
Pfalzner S., 2013, A&A, 549, A82
Pfalzner S., Govind A., 2021, ApJ, 921, 90
Pfalzner S., Vogel P., Scharwächter J., Olczak C., 2005a, A&A, 437, 967
Pfalzner S., Umbreit S., Henning T., 2005b, ApJ, 629, 526
Pichardo B., Sparke L. S., Aguilar L. A., 2005, MNRAS, 359, 521
Porras A., Christopher M., Allen L., Di Francesco J., Megeath S. T., Myers P. C., 2003, AJ, 126, 1916
Portegies Zwart S. F., 2016, MNRAS, 457, 313
Price D. J. et al., 2018, Publ. Astron. Soc. Aust., 35, e031
Principe D. A. et al., 2018, MNRAS, 473, 879
Rein H., Tamayo D., 2015, MNRAS, 452, 376
Ribas Á., Bouy H., Merín B., 2015, A&A, 576, A52

Rodriguez J. E. et al., 2018, ApJ, 859, 150

Rosotti G. P., Dale J. E., de Juan Ovelar M., Hubber D. A., Kruijssen J. M. D., Ercolano B., Walch S., 2014, MNRAS, 441, 2094

Scally A., Clarke C., 2001, MNRAS, 325, 449

Shakura N. I., Sunyaev R. A., 1973, A&A, 24, 337

Shen S., Wadsley J., Hayfield T., Ellens N., 2010, MNRAS, 401, 727

Smallwood J. L., Yang C.-C., Zhu Z., Martin R. G., Dong R., Cuello N., Isella A., 2023, MNRAS, 521, 3500

Steinhausen M., Pfalzner S., 2014, A&A, 565, A32

Takami M. et al., 2018, ApJ, 864, 20

Terquem C., Bertout C., 1996, MNRAS, 279, 415

Thies I., Kroupa P., Goodwin S. P., Stamatellos D., Whitworth A. P., 2010, ApJ, 717, 577

van der Marel N. et al., 2021, AJ, 161, 33

Vincke K., Pfalzner S., 2016, ApJ, 828, 48

Wagner K., Apai D., Kasper M., Robberto M., 2015, ApJ, 813, L2

Weber P. et al., 2023, MNRAS, 518, 5620

Winter A. J., Clarke C. J., Rosotti G., Ih J., Facchini S., Haworth T. J., 2018a, MNRAS, 478, 2700

Winter A. J., Booth R. A., Clarke C. J., 2018b, MNRAS, 479, 5522

Xiang-Gruess M., 2016, MNRAS, 455, 3086

Zurlo A. et al., 2017, MNRAS, 465, 834

APPENDIX A: RESOLUTION STUDY

In Section 4.2, we see that a perturber on a 45°-inclined orbit forms a 90°-inclined protoplanetary disc. Here, we test the resolution to see whether the disc misalignment is robust at higher resolutions. The higher resolution simulation has 4×10^6 particles, eight times more particles than the lower resolution simulations, which constitutes a two-fold increase in resolution.

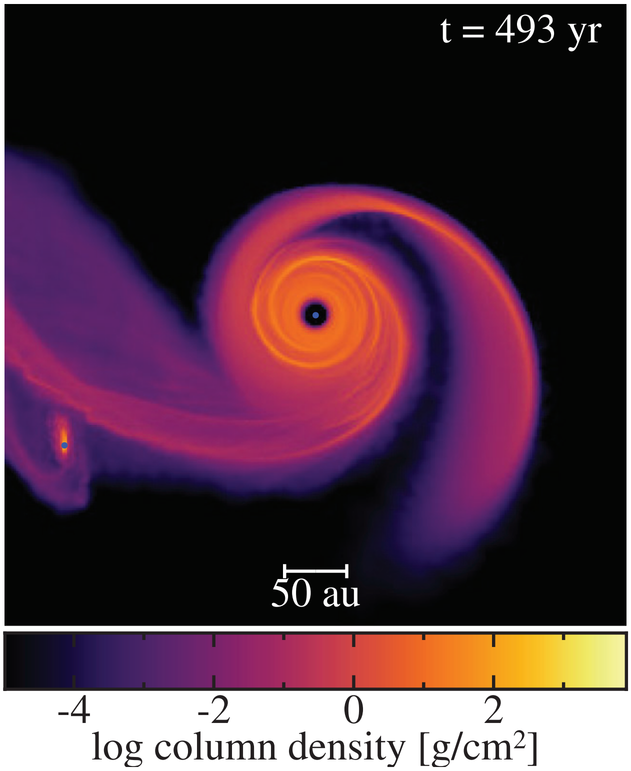

Figure A1. The formation of protoplanetary discs around perturber during a 45°-inclined prograde encounter with high resolution (model H45HR). The frame is centred on the primary star, and viewed in the x–y plane, which is face-on to the primary disc. The image is taken at the same time as the lower resolution image in the top right panel in Fig. 6. The colour denotes the disc surface density.

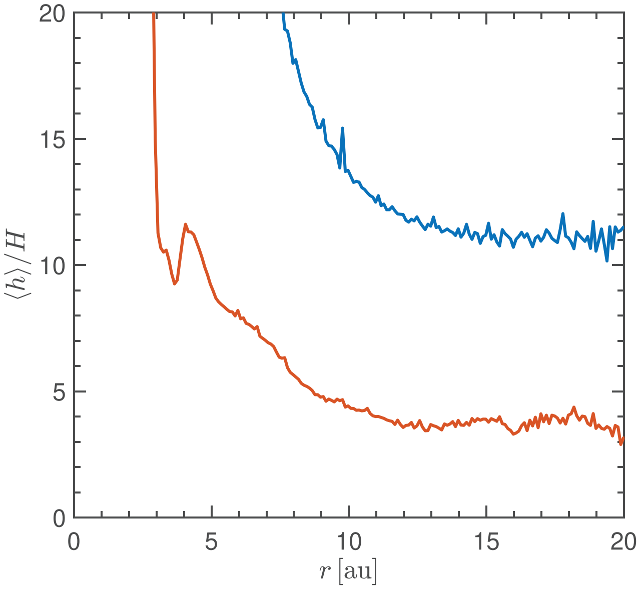

Figure A2. The shell-averaged smoothing length per scale height, $\langle h \rangle/H$, as a function of disc radius, R, for the perturber disc at a time of ∼ 5000 yr. The blue curve represents the low-resolution simulation (500 000 particles, model H45), and the red curve denotes the high-resolution simulation (4×10^6 particles, model H45HR).

Fig. A1 shows the disc surface density for the primary and the perturber discs at a time shortly after the periastron passage of the fly-by for the higher resolution simulation. This image is taken at the same time as the lower resolution image in the top right panel in Fig. 6. The streams accreting on to the perturber disc in the higher resolution simulation are smoother than in the lower resolved simulation.

An important parameter that monitors how resolved discs are is the shell-averaged smoothing length per scale height, $\langle h \rangle/H$. Fig. A2 shows $\langle h \rangle/H$ as a function of the perturber disc radius at a time $t = 5000$ yr. At this time, the perturber disc has damped to twice the initial perturber tilt, which is 90° with respect to the tilt of the primary disc. The blue curve shows the $\langle h \rangle/H$ for the lower resolution simulation, and the red curve shows the $\langle h \rangle/H$ for the higher resolution simulation. For the higher resolution simulation, the forming disc around the fly-by has an overall lower $\langle h \rangle/H$. However, the disc formed in our high resolution simulation is still unresolved since $\langle h \rangle/H$ is still greater than unity. To reach a $\langle h \rangle/H$ value below unity would require roughly 36 times more particles than the higher resolution simulation, which is beyond our computational resources.

APPENDIX B: PHASE ANGLE

In order to achieve a comprehensive characterization of the three-dimensional orientation of the second-generation disc, two angular parameters are essential: the tilt (i) and the longitude of the ascending node (ϕ). This analysis focuses specifically on the ϕ value in each simulation shown in Fig. B1. Notably, simulations featuring a fly-by position angle of zero give rise to second-generation discs that exhibit similar ϕ values. While the ϕ parameter remains relatively stable across these simulations, the disc tilt undergoes changes when the fly-by tilt is varied. Consequently, the disc tilt proves to be a more

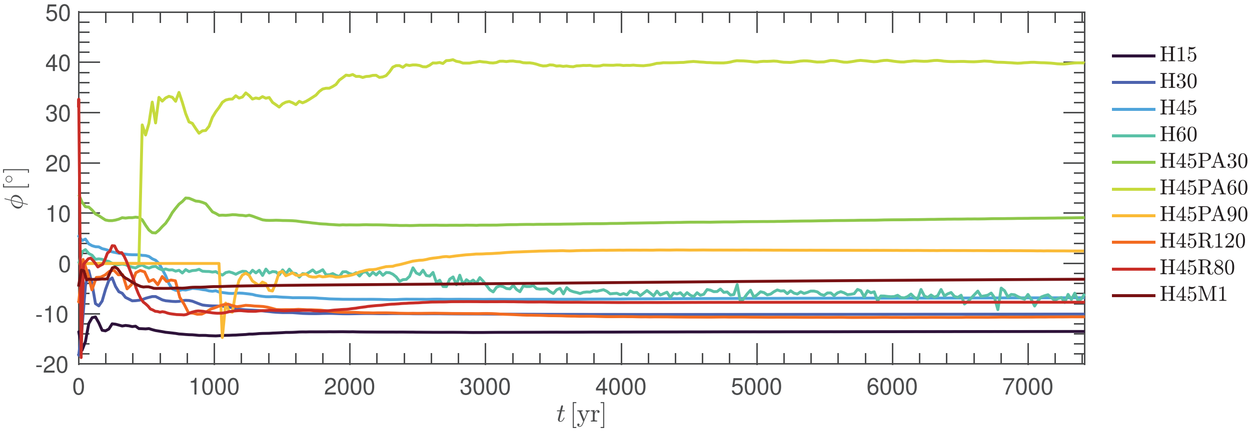

Figure B1. The evolution of the longitude of the ascending node, ϕ, of the disc forming around the perturber for each simulation parameter (given in Table 2) as a function of time. A time $t = 0$ yr represents the time of periastron passage.

valuable parameter for accurately describing the orientation of the fly-by orbit.

APPENDIX C: VELOCITY IMPACT CALCULATIONS

We calculate the velocity perturbations from D'Onghia et al. (2010) using their equations (96)–(107). Here

$$\begin{aligned}\Delta v_x &= -\frac{2GM_2}{B^2V_0} r\{[2\cos\phi_0 - 3A_x]I_{20}(\sqrt{2}\alpha) - 3B_x I_{22}(\sqrt{2}\alpha)\\ &\quad - 3C_x I_{2-2}(\sqrt{2}\alpha)\},\\ \Delta v_y &= -\frac{2GM_2}{B^2V_0} r\{[2\sin\phi_0 - 3A_y]I_{20}(\sqrt{2}\alpha) - 3B_y I_{22}(\sqrt{2}\alpha)\\ &\quad - 3C_y I_{2-2}(\sqrt{2}\alpha)\},\\ \Delta v_z &= -\frac{2GM_2}{B^2V_0} r\{-3A_z I_{20}(\sqrt{2}\alpha) - 3B_z I_{22}(\sqrt{2}\alpha)\\ &\quad - 3C_z I_{2-2}(\sqrt{2}\alpha)\}.\end{aligned} \tag{C1}$$

The generalized Airy functions used in equations (C1) are defined in equations (61)–(62) and (A1)–(A5) of D'Onghia et al. (2010). The terms A_x, B_x,..., C_z are themselves functions of the elements of the rotation matrix used for inclined orbits (section 4, D'Onghia et al. 2010). For our problem, with a rotation of 90° around the z-axis followed by θ around the y-axis, the rotation matrix reduces to

$$\tilde{A} = \begin{bmatrix} 0 & -\cos\theta & \sin\theta \\ 1 & 0 & 0 \\ 0 & \sin\theta & \cos\theta \end{bmatrix}. \tag{C2}$$

Thus the above constants are transformed to

$$\begin{aligned}A_x &= \cos^2\theta\cos\phi_0,\\ B_x &= 0.5(\cos\theta - \cos^2\theta)\cos\phi_0,\\ C_x &= 0.5(-\cos\theta - \cos^2\theta)\cos\phi_0,\\ A_y &= \sin\phi_0,\\ B_y &= 0.5(1 - \cos\theta)\sin\phi_0,\\ C_y &= 0.5(1 + \cos\theta)\sin\phi_0,\\ A_z &= -\cos\theta\cos\phi_0\sin\theta,\\ B_z &= 0.5\cos\phi_0(-\sin\theta + \cos\theta\sin\theta),\\ C_z &= 0.5\cos\phi_0(\sin\theta + \cos\theta\sin\theta).\end{aligned} \tag{C3}$$

Recall here that ϕ_0 is the phase angle during periapsis passage.

This paper has been typeset from a TEX/LATEX file prepared by the author.